UC Irvine

UC Irvine Previously Published Works

Title

Multi-Wavelength Photo-Magnetic Imaging System for Photothermal Therapy Guidance

Permalink

https://escholarship.org/uc/item/71d4h3km

Journal

Lasers in Surgery and Medicine, 53(5)

ISSN

1050-9267

Authors

Algarawi, Maha
Erkol, Hakan
Luk, Alex
et al.

Publication Date

2021-07-01

DOI

10.1002/lsm.23350

Peer reviewed

eScholarship.org Powered by the California Digital Library
University of California

Author Manuscript

Author Manuscript

Author Manuscript

Author Manuscript

HHS Public Access

Author manuscript

Lasers Surg Med. Author manuscript; available in PMC 2022 July 01.

Published in final edited form as:

Lasers Surg Med. 2021 July ; 53(5): 713–721. doi:10.1002/lsm.23350.

Multi-Wavelength Photo-Magnetic Imaging System for Photothermal Therapy Guidance

Maha Algarawi[1,2], **Hakan Erkol**[3], **Alex Luk**[1], **Seunghoon Ha**[4], **Mehmet Burcin Unlu**[3], **Gultekin Gulsen**[1,2,5], **Farouk Nouizi, PhD**[1,5,*]

[1]Center for Functional Onco-Imaging, University of California Irvine, Irvine, California 92697, USA

[2]Department of Physics and Astronomy, University of California Irvine, Irvine, California 92697, USA

[3]Department of Physics, Bogazici University, Istanbul, 34342, Turkey

[4]Philips Healthcare, Pewaukee, Wisconsin 53072, USA

[5]Department of Radiological Sciences, University of California Irvine, Irvine, California 92697, USA

Abstract

Background and Objectives: In photothermal therapy, cancerous tissue is treated by the heat generated from absorbed light energy. For effective photothermal therapy, the parameters affecting the induced temperature should be determined before the treatment by modeling the increase in temperature via numerical simulations. However, accurate simulations can only be achieved when utilizing the accurate optical, thermal, and physiological properties of the treated tissue. Here, we propose a multi-wavelength photo-magnetic imaging (PMI) technique that provides quantitative and spatially resolved tissue optical absorption maps at any wavelength within the near-infrared (NIR) window to assist accurate photothermal therapy planning.

Study Design/Materials and Methods: The study was conducted using our recently developed multi-wavelength PMI system, which operates at four laser wavelengths (760, 808, 860, and 980 nm). An agar tissue-simulating phantom containing water, lipid, and ink was illuminated using these wavelengths, and the slight internal laser-induced temperature rise was measured using magnetic resonance thermometry (MRT). The phantom optical absorption was recovered at the used wavelengths using our dedicated PMI image reconstruction algorithm. These absorption maps were then used to resolve the concentration of the tissue chromophores, and thus deduce its optical absorption spectrum in the NIR region based on the Beer–Lambert law.

Results: The optical absorption of the phantom was successfully recovered at the used four wavelengths with an average error of ~1.9%. The recovered absorption coefficient was then used to simulate temperature variations inside the phantom. A comparison between the modeled temperature maps and the MRT measured ones showed that these maps are in a good agreement

*Correspondence to: Farouk Nouizi, PhD, Center for Functional Onco-Imaging, University of California Irvine, Irvine, California, 92697, USA. fnouizi@uci.edu.

Conflict of Interest Disclosures: All authors have completed and submitted the ICMJE Form for Disclosure of Potential Conflicts of Interest and none were reported.

Author Manuscript Author Manuscript Author Manuscript Author Manuscript

with an average pseudo R^2 statistic of 0.992. These absorption values were used to successfully recover the concentration of the used chromophores. Finally, these concentrations are used to accurately calculate the total absorption spectrum of the phantom in the NIR spectral window with an average error as low as ~2.3%.

Conclusions: Multi-wavelength PMI demonstrated a great ability to assess the distribution of tissue chromophores, thus providing its total absorption at any wavelength within the NIR spectral range. Therefore, applications of photothermal therapy applied at NIR wavelengths can benefit from the absorption spectrum recovered by PMI to determine important parameters such as laser power as well as the laser exposure time needed to attain a specific increase in temperature prior to treatment.

Keywords

photo-magnetic imaging; photothermal therapy; magnetic resonance thermometry; finite element method; image reconstruction; multi-wavelength lasers

INTRODUCTION

Laser photothermal therapy (PTT) is a medical technique that utilizes light to irradiate biological tissue for cancer treatment. During the therapy, laser light is absorbed by the medium causing a temperature elevation due to the conversion of photon energy into heat [1]. PTT can be divided into two forms: low-temperature hyperthermia and thermolysis. Hyperthermia occurs by heating up the biological tissue 6–8°C. Heating the tissue up to this level would change the tumor microenvironment, and alter blood flow and oxygen distribution within the tumor, leading to cancer cell death by apoptosis [2,3]. For thermolysis, laser is applied to heat the tumor to more than 13°C, which causes a tumor destruction by necrosis [4,5].

In both PTT regimes, the efficacy of the treatment depends on the accuracy and performance of the heat delivery method. Therefore, adjusting experimental parameters that control the temperature elevation such as laser settings and exposure time is crucial. Indeed, determining these parameters is critical to avoid overheat during hyperthermia, and insufficient heating during thermolysis. Hence, a customized thermal protocol should be developed to attain these parameters prior to the treatment throughout simulation studies [6]. These simulation studies are generally performed through the modeling of the spatiotemporal distribution of temperature-induced by tissue light absorption using the bio-heat equation [7–11].

For an effective PTT, exogenous agents are frequently utilized to enhance light absorption at the tumor; consequently, the temperature selectively increases within tumor cells with minimal collateral damage to healthy tissue [12–14]. Gold nanoparticles having a tunable absorption bandwidth as well as Food and Drug Administration-approved indocyanine green (ICG) have been used in different studies as exogenous agents to increase light absorption during thermal treatment [15–20]. Therefore, in addition to the tumor local absorption, the increase in absorption due to these exogenous agents needs to be accurately defined before performing PTT to attain an accurate temperature modeling.

Author Manuscript Author Manuscript Author Manuscript Author Manuscript

Conventional diffuse optical techniques have been widely used to recover optical properties of biological tissue [21–23]. However, standard diffuse optical modalities alone yield absorption maps with low spatial resolution resulting in poor quantitative accuracy [24]. Studies showed that integrating these techniques with anatomical imaging modalities would improve their performance [25]. However, these techniques were limited to using structural information obtained by the anatomical imaging technique to constrain the image reconstruction algorithm of the diffused optical imaging technique.

Recently, our team introduced a truly hybrid technique termed, photo-magnetic imaging (PMI). PMI is a non-invasive high-resolution imaging technique that accurately provides tissue optical absorption and overcomes several limitations of conventional diffuse optical imaging techniques. The superior performance of PMI has been proven using numerous simulation and experimental studies [26–31]. In PMI, a continuous wave laser is applied to induce a slight increase of temperature in the imaged tissue. This temperature increase is governed by the maximum permissible exposure limits for skin, which is defined by the American National Standards Institute (ANSI). PMI non-invasively monitors the evolution of the laser-induced temperature using magnetic resonance thermometry (MRT) [32]. MRT provides high-resolution maps of the internal variations of temperature, which can be converted to high-resolution optical absorption maps using our dedicated PMI image reconstruction algorithm [26,30]. This algorithm consists of two steps, namely the PMI forward and inverse problems. During the forward problem, simulated temperature maps are generated by first modeling the light propagation through the tissue using the diffusion equation [33–35]. Second, the density of light within the tissue is converted to heat and utilized to model the temperature increase and propagation using the Pennes bio-heat equation [26,32]. Later, the high-resolution absorption maps are reconstructed by iteratively minimizing an error objective function of the MRT and the simulated temperature maps, during the resolution of the inverse problem [26,27].

PMI has the potential to become a valuable tool for PTT applications by non-invasively providing the optical absorption of the treated tissue with high-resolution and quantitative accuracy. Technically, the total tissue absorption corresponds to the sum of absorptions of all its chromophores, including oxy-hemoglobin, deoxy-hemoglobin, water, fat as well as the accumulated exogenous agent [36]. Assessing the contribution of each of these chromophores through their concentration is crucial. Therefore, PMI has been upgraded from single to multiple wavelengths to recover the chromophore concentration with high-resolution and quantitative accuracy [37]. Determining the chromophore concentrations allows to deduce the total absorption spectrum of tissue within the near-infrared (NIR) spectral range based on the modified Beer–Lambert law [38]. Therefore, PMI can be used prior to PPT applications to provide spatially resolved and quantitatively accurate total absorption of the tissue to be treated and assist in the determination of the optimal experimental parameters such as laser power and exposure time.

In this paper, we present preliminary results obtained using our novel multi-wavelength PMI system that uses four NIR laser diodes (760, 808, 860, and 980 nm). PMI was used to recover the optical absorption coefficient of a tissue-simulating phantom at these wavelength. The recovered absorption coefficients at each wavelength were then used to

Author Manuscript Author Manuscript Author Manuscript Author Manuscript

obtain the concentration of the main chromophores of the phantom, thus deducing its total absorption spectrum.

MATERIALS AND METHODS

Instrumentation

Our multi-wavelength PMI system was entirely home-built. The system mainly consists of high-power lasers and their drivers, a temperature management system, and a control computer. To accommodate the tight space inside the MRI control room, the system was designed to fit inside a compact 18″ × 24″ × 32″ mobile cart (Fig. 1a). The multi-wavelength PMI system is designed to operate at four different laser wavelengths: 760 nm (5 W; LDX Optronics Inc., Maryville, TN, US), 808 nm (7 W; Focuslight Inc., Xi'an, China), 860 nm (4.6 W; LDX Optronics Inc., Maryville, TN, US), and 980 nm (4.5 W; LDX Optronics Inc., Maryville, TN, US). To allow heating the subject from multiple sides, four laser diodes are used at each wavelength. Each laser diode is driven with a dedicated laser diode driver (PLD5000; Wavelength Electronics Inc., Bozeman, MT, US). The laser drivers are grouped according to their operating wavelength and installed at the top of the system allowing users an easy access at any time.

As our system employs high-power laser diodes, the increase in their operating temperature is inevitable. High operating temperature would cause a shift in the laser operating wavelength and a decrease in the laser diode lifetime. Therefore, a Temperature Management System was implemented to monitor and control the operating temperature of the lasers (Fig. 1b). First, the laser diodes are mounted on copper plates to dissipate the generated operating heat. The copper plates are directly placed in contact with a group of thermoelectric cooling (TEC) units (TEC1-12706; Hebei I. T. Co., Shanghai, China), which transfer the heat down to a fan-cooled heat sink. The temperature of the copper plate is continuously measured using a thermistor (TH10K; Thorlabs Inc., Newton, NJ, US) and used as feedback for a proportional–integral–derivative temperature control closed-loop controller.

A 3 Tesla MRI system (Achieva; Philips, Pewaukee, WI, US) was used to perform MRT measurements and monitor the internal temperature increase inside the imaged phantom. To acquire high signal-to-noise-ratio MRT images, a small animal home-built radio frequency (RF) coil was used to acquire the MR signals while holding the phantom [32]. This RF coil was also designed to allow illumination of the phantom through four windows to perform multi-site heating [27]. Each of these windows accommodated the tip of one of the four optical fibers (ϕ = 1 mm, 15-m-long) used to transport light from the PMI cart located in the control room to the RF coil inside the MRI bore. To perform a uniform illumination at the phantom surface, light is collimated using a collimation lens (35 mm; Newport Corporation, Irvine, CA, US) (Fig. 1b). Finally, to accommodate all the input and output signals in our system, four data acquisition units were used: two DAQ cards (6023E and 6703) and two DAQ USB-6008. A LabVIEW program was implemented to control all the operating functionalities automatically (monitor and adjust the laser current, acquire temperature feedback, control the TEC units and fans, and manage the alarms).

Author Manuscript Author Manuscript Author Manuscript Author Manuscript

PMI Image Reconstruction Algorithm

PMI forward problem.—In the PMI forward problem, the simulated temperature maps are obtained by solving a system of two equations using the Finite Element Method [26]. First, the photon propagation in the medium is modeled using the diffusion equation and the Neumann boundary conditions [34,35,39,40,41]:

$$\begin{Bmatrix} -\nabla[D^{\lambda}(r)\nabla\phi^{\lambda}(r)] + \mu_a^{\lambda}(r)\phi^{\lambda}(r) = S^{\lambda}(r) \\ \overrightarrow{n}\, D\nabla\phi(r) + A\phi(r) = 0 \end{Bmatrix} \quad (1)$$

where $\phi(r)[\mathrm{W\cdot mm^{-2}}]$ is the photon density at position r [mm], D [mm] is the diffusion coefficient, $D(r) = \frac{1}{3(\mu_a + \mu'_s)}$, μ_a [$\mathrm{mm^{-1}}$] and $\mu'_s\left[\mathrm{mm^{-1}}\right]$ are the absorption and reduced scattering coefficients, respectively. λ denotes the used laser wavelength. S [$\mathrm{W\cdot mm^{-3}}$] is the isotropic source of light. $\overrightarrow{n}$ is the normal vector to the surface and A is the reflection coefficient at the surface [35].

The photon density $\phi(r)$ resulted from the diffusion equation is used to calculate the source of thermal energy induced by the laser [26,32]:

$$Q_R(r) = \mu_a^{\lambda}(r)\phi^{\lambda}(r) \quad (2)$$

Second, the source of heat Q_R is then used in the heat conduction equation to model the heat propagation in the tissue [28,42]:

$$\begin{Bmatrix} \rho c\frac{\partial T(r,t)}{\partial t} - \nabla[k\nabla T(r,t)] = Q_R \\ -k\frac{\partial T(r)}{\partial n} = h[T_f - T(r)] \end{Bmatrix} \quad (3)$$

where ρ is the density, c is the specific heat, and k is the thermal conductivity of the tissue. Q_R is the thermal energy source. The second equation describes the heat convection boundary condition, where h is the heat transfer coefficient and T_f is the ambient temperature.

PMI inverse problem.—The inverse problem of PMI consists in minimizing the quadratic error between the measured MRT temperature and the simulated temperature maps from the forward problem solver. Here, the inverse problem is solved by iteratively minimizing the following objective function:

$$\Omega(\mu_a) = \sum \left\| T^m - T(\mu_a) \right\|^2 \quad (4)$$

where T^m is the measured MRT temperature maps and T is the simulated temperature map calculated by the forward problem solver using the absorption spatial distribution μ_a [26,27].

Once the tissue optical absorption is obtained at the used wavelengths, the modified Beer–Lambert Law is used to recover the concentration of its chromophores:

Author Manuscript Author Manuscript Author Manuscript Author Manuscript

$$\mu_a(\lambda) = \sum_{i=1}^{N_c} \mu_{ai}(\lambda) = \ln 10 \sum_{i=1}^{N_c} \varepsilon_i \, . \, C_i \tag{5}$$

where μ_a is the wavelength-dependent absorption coefficient of the tissue, N_c is the number of chromophores, ε_i and C_i are the wavelength-specific extinction coefficient and concentration of an individual chromophore i, respectively.

MRT

The proton resonance frequency (PRF) method is one of the MRT techniques. PRF is highly sensitive to temperature variations [43]. Changes in the PRF induces a variation in the measured MR phase measurements, which are proportional to temperature variations:

$$\Delta T = \frac{\psi(t) - \psi(t_0)}{\gamma \alpha B_0 T_E} \tag{6}$$

where $\psi(t)$ is the measured phase at time t, $\psi(t_0)$ is the baseline phase measured at a known temperature at time t_0, γ is the gyromagnetic ratio (42.58 MHz/T for hydrogen), α is the coefficient relating phase change to temperature (−0.009 ppm/°C for biotissue), B_0 is the local magnetic field (3 T), and T_E is the MRT echo time (12 milliseconds) [44]. Figure 2 displays the data acquisition timeline showing the laser status and the change in temperature of the tissue during two different periods: baseline and heating periods. t_0 and t_H are the times needed to acquire all the frames within the baseline and heating period, respectively.

Each period consists of multiple frames with a duration defined by the MRT imaging parameters. In this study, 320 × 320 pixels^2 MRT images, with a pixel size of 0.1875 mm, are acquired using a gradient-echo sequence with repetition time T_R = 82 milliseconds, T_E = 12 milliseconds, and a flip angle of 22° resulting in a temporal resolution of 6 seconds. First, the baseline phase maps are acquired before turning ON the laser $\psi(t_0)$. Next, the laser is turned ON and the heating phase maps $\psi(t_H)$ are recorded. The internal laser-induced temperature variation is then obtained using Equation (6).

Phantom Studies

The phantom used in this study is a mice-sized (25 mm diameter and 100mm height) cylindrical homogenous agar phantom. For this study, the phantom was aligned along the MRI axial direction. A single illumination window is used to heat-up the phantom from its top side. The phantom axial dimension center was aligned with the laser spot center. Figure 3 illustrates a T1-weighted MR image showing a cross-section of the phantom and the laser source position. The laser output power is measured for each laser wavelength by a power meter (PM10-10; Thorlabs Inc., Newton, NJ, US) and set to 1.5 W. Considering that the laser spot size is approximately 1.3 cm in diameter, the resultant power density was 1.13 W·cm^{-2}.

The phantom optical properties were set using Intralipid and black Indian ink dye for scattering and absorption adjustment, respectively. The total absorption coefficient of the

Author Manuscript Author Manuscript Author Manuscript Author Manuscript

phantom consists in the sum of absorptions of its main chromophores (water, intralipid, and the ink dye), and will be referred to as real absorption of the phantom through the paper (Fig. 4) [37,38,45]. The absorption spectra of both water and lipid were obtained from the literature [46,47]. The optical absorption spectrum of the ink dye was experimentally measured using a spectrometer (USB 2000+; Ocean Optics, Inc., Dunedin, FL, US).

The reduced scattering coefficient of the phantom was adjusted using intralipids and set to be equal to 0.89 mm^{-1} at 760 nm and validated using our frequency-domain diffuse optical tomography (DOT) system [48]. The values for the other wavelengths were calculated using the Mie theory approximation [49]. The phantom optical properties are summarized in Table 1.

The thermal properties of the phantom were set to be the same as water values since it represented approximately 98% of its constituents, Table 2 [50].

RESULTS

The MRT acquisition of the laser-induced temperature distribution was performed for 12 seconds, which resulted in two MRT frames during the heating period. The MRT temperature maps were sequentially acquired for each wavelength. A 2 minutes gap was always used between acquisitions to ensure that the entire heat from the previous heating had dissipated and that the phantom went back to its baseline temperature. The experiment was conducted at an ambient temperature of 20°C. The first row of Figure 5 shows the second MRT frame measured temperature maps at each wavelength after a 12 seconds heating period.

In this experiment, the phantom was only illuminated from its top side inducing a higher increase in temperature below the illumination site. The increase of temperature depends on several parameters such as the applied laser power, exposure time, and optical properties of the phantom. In this study, the applied power and the exposure time were set to be equal for all wavelengths; therefore, any temperature increase difference would be due to differences in the optical absorption coefficient of the phantom. At the first three wavelengths (760, 808, and 860 nm), a comparable temperature increase was observed with a peak increase of 1.33°C. This similarity in the temperature variation is an indication of having a relatively similar absorption at these wavelengths. However, a higher increase in temperature was observed at 980 nm. This high-temperature increase at this wavelength is mainly due to the absorption of water, which has its absorption peak at 980 nm [47]. PMI was used to resolve the phantom optical absorption coefficient at each wavelength using the MRT measured temperature maps. PMI recovered a homogeneous absorption map at each wavelength, (Table 3).

The absorption values summarized in Table 3 demonstrate the ability of PMI to accurately recover the optical absorption of the phantom with an average error as low as ~1.9%. As expected from the MRT temperature maps, Table 3 shows that the recovered absorption coefficients are relatively similar at the first three wavelengths (760, 808, and 860 nm) while it is approximately five times higher at 980 nm.

Author Manuscript Author Manuscript Author Manuscript Author Manuscript

To validate our results, the recovered absorption coefficients (Table 3) were used in Equation (1) to calculate the photon density distribution within a numerical phantom having the same dimensions as the experimental one. Next, the solution of Equation (1) was used in Equation (3) to generate the simulated temperature maps. Solving these two equations system allows to generate temperature distributions at defined times. However, each MRT frame requires 6 seconds to be acquired, yielding to the fact that the recorded MRT temperature corresponds to the mean temperature increase during the 6 seconds frame duration and not the temperature at the end of the frame. Therefore, the generated simulated temperatures were first averaged overtime periods corresponding to the MRT duration frames before being compared with MRT experimental data. The simulated temperature map corresponding to the mean of the temperatures between a 7 and 12 seconds heating period (second MRT frame) at each wavelength is presented in the second row of Figure 5.

These simulated temperature maps show the same temperature variations as the MRT measured ones. A performance validation was achieved by comparing the temperature change at each point of the experimental data with the simulated ones. Figure 6 presents a profile carried-out along the *y*-axis of the MRT temperature maps (red lines) and the simulated ones (blue lines) at each wavelength. The blue highlighted region illustrates the noise level of our MRT measurements which is equal to 0.1°C [27].

These results confirmed that the simulated temperature profiles are in a good agreement with the measured MRT ones with a pseudo R^2 statistic as good as 0.992 on average for all wavelengths. Our PMI forward problem was also extensively validated in our previous works [10,26,27,28,32,51].

The recovered optical absorption at the used four wavelengths was then utilized in the modified Beer–Lambert Law to retrieve the concentration of the main chromophores of the phantom using a least-squared minimization process. The contribution of the absorption of lipids was neglected as their absorption at the used wavelengths represent less than 2.2% of the total absorption of the phantom. Table 4 summarizes the real and recovered concentration values of both water and the ink dye.

The concentration maps were recovered accurately with an average error of 0.4% and 11.4% for the water and the used ink dye, respectively. Finally, the recovered concentration values of the main chromophores were used to calculate the total absorption spectrum of the phantom in the NIR window using Equation (5). Figure 7 shows the calculated total absorption of the phantom in the NIR spectral range.

These recovered total absorption of the phantom would be highly beneficial during PPT planning to accurately determine the optimal experimental parameters required to achieve a desired heating depending on the patient needs prior to the therapy.

DISCUSSION

Conventional diffuse optical imaging techniques have been widely used to recover the main biotissue chromophore concentration [52–55]. However, the recovered concentration maps

Author Manuscript Author Manuscript Author Manuscript Author Manuscript

using these techniques suffer from low resolution, which consequently results in poor quantitative accuracy.

Recently, PMI has been proposed to overcome the limited resolution of the conventional diffuse optical techniques. PMI was designed as a safe optical imaging modality that can provide high-resolution optical absorption maps from laser-induced temperature distribution measurements. In this study, we upgraded the single wavelength prototype to a multi-wavelength full version that utilizes four laser wavelengths (760, 808, 860, and 980 nm). These laser wavelengths were carefully chosen to recover the concentration of oxy- and deoxy-hemoglobin, and water. This approach is based on the fact that each of these chromophores has a unique absorption spectrum. Single-wavelength PMI was previously validated using both simulation and experimental studies. Here, our aim was to leverage the important information that can be retrieved by the multi-wavelength approach. Using a limited number of laser wavelengths, PMI can assess the concentration of the main tissue chromophores, and thus provide the total tissue absorption spectrum within the NIR spectral range. This information is crucial to the performance of accurate PTT planning through numerical modeling.

For this phantom experiment, the laser output power used for all wavelengths was set to 1.5 W, while the diameter of the laser spot was 1.3 cm. Hence, the power density was equal to 1.13 W/cm^2. This power density was approximately 4.3, 3.4, 2.7, and 1.6 times higher than the maximum permissible exposure (MPE) for laser wavelengths 760, 808, 860, and 980 nm, respectively. Please note that for future *in vivo* applications, the MPE limits can be easily achieved by adjusting the laser power, using our computer-controlled laser driver system, and/or by increasing the spot size. Nevertheless, PMI has various applications and can be used to image larger tissue, as for breast imaging. Larger tissue needs the use of high-power levels to perform large area illumination and achieve sufficient heating. Therefore, our system was equipped with high-power lasers to elevate the internal temperature few degrees without altering the physiological process in the body or causing any thermal damage. PMI temperature measurements are acquired in a few seconds after turning on the laser to induce a slight increase in the tissue internal temperature. The temperature change has to be higher than the MRT noise level (0.1°C), but lower than hyperthermia to avoid protein denaturation. Therefore, for PMI *in vivo* studies, the MPE limits for skin must be calculated and respected for each laser wavelength.

In this study, our multi-wavelength PMI system was used to determine the optical absorption coefficient of a tissue-mimicking phantom at four wavelengths. The absorption values were accurately recovered with an average error as low as ~1.9%. These recovered optical absorptions at different wavelengths were then used in the PMI forward problem to simulate the change in temperature. The results in Figure 6 showed that simulated temperatures were in a good agreement with the measured MRT ones with an average pseudo R^2 of 0.992. These optical absorption values recovered at the used four wavelengths were employed to obtain the concentration of the main chromophores. By neglecting the lipids contributions, the water and ink dye concentration values were, respectively, recovered with an average error as low as 0.4% and 11.4%. These recovered concentration values were then used to deduce the total phantom absorption spectrum. As observed on Figure 7, the recovered total

Author Manuscript Author Manuscript Author Manuscript Author Manuscript

absorption spectrum is in a good agreement with the real one with an average error of ~2.3%, except in the spectral region around 930 nm. This spectral region corresponds to the peak absorption of lipids, which were neglected during the concentration calculations. This error clearly shows that a laser wavelength is required for each specific chromophore based on its peak absorption. Therefore, our system was designed to host two additional lasers. Wavelength 930 nm will be added to be able to recover the concentration of lipids. Also, we plan to add another wavelength in order to recover an exogenous contrast agent. This wavelength will be chosen once we establish which agent will be used.

Although demonstrating a high performance, PMI remains limited due to several factors. For example, the thermal properties were assumed to be equal to those of water and homogeneously attributed to the entire phantom. For *in vivo* applications, the T1-weighted anatomical image, acquired before the MRT maps, will be segmented to define different organs regions and use their specific thermal properties based on the literature values. Also, *in vivo* imaging will require upgrading the modeling process by using the bio-heat equation in order to account for tissue perfusion. Another limitation results from the fact that the reduced scattering coefficient was set using intralipids according to our established phantom preparation protocol and validated using our DOT system. For PMI to be a stand-alone modality, we are implementing an updated version of the PMI image reconstruction algorithm that also allows obtaining the spatially resolved scattering coefficient from the multi-wavelength MRT maps based on the method proposed by Cho et al. [55].

CONCLUSION

In summary, we designed and built a multi-wavelength PMI system that utilizes four laser wavelengths in the NIR range. The performance of our system was experimentally validated utilizing an agar tissue-simulating phantom. The phantom had different absorption coefficients at the used four wavelengths due to its constituent's absorption spectra. The experiment consisted in heating the phantom at each wavelength and measuring the spatiotemporal induced temperature distribution using MRT. Then, the optical absorption coefficient of the phantom was determined at each wavelength using the PMI image reconstruction algorithm. Using the PMI recovered optical absorption coefficients, the performance was later validated by comparing the simulated and measured laser-induced temperature maps. The results showed that simulated temperatures were in a good agreement with the measured MRT ones with an average pseudo R^2 of 0.992.

By probing the phantom at certain wavelengths, the concentration values of its main chromophores were successfully recovered. Obtaining chromophore concentration values allows obtaining the total absorption of the phantom at any wavelength with an average error as low as ~2.3%. Consequently, multi-wavelength PMI has the potential to be used prior to PTT to provide the initial optical absorption of the tissue at the suitable laser wavelength used in the treatment and assist in the determination of key experimental parameters such as laser power and exposure time.

Author Manuscript Author Manuscript Author Manuscript Author Manuscript

ACKNOWLEDGMENTS

This research is supported in part by a scholarship awarded to Maha Algarawi from the Department of Physics, Imam Mohammad Ibn Saud Islamic University (IMISU), a Fulbright grant awarded to Farouk Nouizi, the National Institutes of Health (NIH) R01EB008716, R33CA120175, P30CA062203, R21CA170955, the Ruth L Kirschstein National Research Service Award (F31) F31CA171915-01A1, the Susan G Komen Foundation training grant: KG101442, TUBITAK (2009K120520), and Bogazici University (BAP 15362).

REFERENCES

1. Yun SH, Kwok SJJ. Light in diagnosis, therapy and surgery. Nat Biomed Eng 2017;1(1):1–16.
2. Mantso T, Goussetis G, Franco R, Botaitis S, Pappa A, Panayiotidis M. Effects of hyperthermia as a mitigation strategy in dna damage-based cancer therapies. Semin Cancer Biol 2016;37:96–105. [PubMed: 27025900]
3. Terentyuk GS, Ivanov AV, Polyanskaya NI, et al. Photothermal effects induced by laser heating of gold nanorods in suspensions and inoculated tumours during in vivo experiments. Quantum Elec 2012;42(5):380.
4. Goldberg SN, Gazelle GS, Mueller PR. Thermal ablation therapy for focal malignancy: A unified approach to underlying principles, techniques, and diagnostic imaging guidance. Am J Roentgenol 2000;174(2):323–331. [PubMed: 10658699]
5. Stafford RJ, Fuentes D, Elliott AA, Weinberg JS, Ahrar J. Laser-induced thermal therapy for tumor ablation. Crit Biomed Eng 2010;38:79–100.
6. Shafirstein G, Feng Y. The role of mathematical modelling in thermal medicine. Int J Hyperthermia 2013;29(4):259–261. [PubMed: 23738694]
7. Manuchehrabadi N, Chen Y, LeBrun A, Ma R, Zhu L. Computational simulation of temperature elevations in tumors using monte carlo method and comparison to experimental measurements in laser photothermal therapy. J Biomech Eng 2013;135(12):121007. [PubMed: 24026290]
8. Mohammed Y, Verhey JF. A finite element method model to simulate laser interstitial thermo therapy in anatomical inhomogeneous regions. Biomed Eng Online 2005;4(1):2. [PubMed: 15631630]
9. Xu Y, Long S, Yang Y, et al. Mathematical simulation of temperature distribution in tumor tissue and surrounding healthy tissue treated by laser combined with indocyanine green. Theor Biol Med Model 2019;16(1):1–11. [PubMed: 30642334]
10. Erkol H, Nouizi F, Luk A, Unlu MB, Gulsen G. Comprehensive analytical model for cw laser induced heat in turbid media. Optics Express 2015;23(24):31069–31084. [PubMed: 26698736]
11. Erkol H, Yelken SZ, Algarawi M, Gulsen G, Nouizi F. Validation of a comprehensive analytical model for photothermal therapy planning in a layered medium with gold nanoparticles. Int J Heat Mass Trans 2020;163:120438.
12. Schwartz JA, Shetty AM, Price RE, et al. Feasibility study of particle-assisted laser ablation of brain tumors in orthotopic canine model. Cancer Res 2009;69(4):1659–1667. [PubMed: 19208847]
13. Loo C, Lowery A, Halas N, West J, Drezek R. Immunotargeted nanoshells for integrated cancer imaging and therapy. Nano Lett 2005;5(4):709–711. [PubMed: 15826113]
14. Mallidi S, Anbil S, Bulin A-L, Obaid G, Ichikawa M, Hasan T. Beyond the barriers of light penetration: Strategies, perspectives and possibilities for photodynamic therapy. Theranostics 2016;6(13):2458. [PubMed: 27877247]
15. Goodrich GP, Bao L, Gill-Sharp KL, Sang KL, Wang JC, DonaldPayne J. Photothermal therapy in a murine colon cancer model using near-infrared absorbing gold nanorods. J Biomed Opt 2010;15(1):018001. [PubMed: 20210487]
16. Kennedy LC, Bickford LR, Lewinski NA, et al. A new era for cancer treatment: Gold-nanoparticle-mediated thermal therapies. Small 2011;7(2):169–183. [PubMed: 21213377]
17. O'Neal DP, Hirsch LR, Halas NJ, Payne JD, West JL. Photothermal tumor ablation in mice using near infrared-absorbing nanoparticles. Cancer Lett 2004;209(2):171–176. [PubMed: 15159019]

Author Manuscript Author Manuscript Author Manuscript Author Manuscript

18. Chen Y, Gnyawali SC, Wu F, et al. Magnetic resonance imaging guidance for laser photothermal therapy. J Biomed Opt 2008;13(4):044033. [PubMed: 19021360]
19. Taylor JS, Zeki J, Ikegaki N, Chen LL, Chiu B. Combined application of indocyanine green (icg) and laser lead to targeted tumor cell destruction. J Pediatr Surg 2018; 53(12):2475–2479. [PubMed: 30244940]
20. Long S, Xu Y, Zhou F, et al. Characteristics of temperature changes in photothermal therapy induced by combined application of indocyanine green and laser. Oncol Lett 2019; 17(4):3952–3959. [PubMed: 30930992]
21. Sekar SKV, Farina A, Mora AD, et al. Broadband (550-1350 nm) diffuse optical characterization of thyroid chromophores. Sci Rep 2018;8(1):1–8. [PubMed: 29311619]
22. Durduran T, Choe R, Culver JP, et al. Bulk optical properties of healthy female breast tissue. Phys Med Biol 2002;47(16):2847. [PubMed: 12222850]
23. Xu Y, Iftimia N, Jiang H, Key LL, Bolster MB. Imaging of in vitro and in vivo bones and joints with continuous-wave diffuse optical tomography. Opt Express 2001;8(7):447–451. [PubMed: 19417840]
24. Arridge SR, Lionheart WRB. Nonuniqueness in diffusion-based optical tomography. Opt Lett 1998;23(11):882–884. [PubMed: 18087373]
25. Kwong TC, Hsing M, Lin Y, et al. Differentiation of tumor vasculature heterogeneity levels in small animals based on total hemoglobin concentration using magnetic resonance-guided diffuse optical tomography in vivo. Appl Opt 2016;55(21):5479–5487. [PubMed: 27463894]
26. Lin Y, Gao H, Thayer D, Luk AL, Gulsen G. Photo-magnetic imaging: Resolving optical contrast at mri resolution. Phys Med Biol 2013;58(11):3551. [PubMed: 23640084]
27. Nouizi F, Luk AT, Thayer D, Lin Y, Ha S, Gulsen G. Experimental validation of a high-resolution diffuse optical imaging modality: photomagnetic imaging. J Biomed Opt 2016;21(1):016009.
28. Luk A, Nouizi F, Erkol H, Unlu MB, Gulsen G. Ex vivo validation of photo-magnetic imaging. Opt Lett 2017;42(20):4171–4174. [PubMed: 29028040]
29. Luk AT, Nouizi F, Marks M, Kart T, Gulsen G. Monitoring gold nanoparticle distribution with high resolution using photo-magnetic imaging. Optical Interactions With Tissue and Cells XXVII, 9706, 97060M. International Society for Optics and Photonics; 2016.
30. Nouizi F, Erkol H, Luk A, Marks M, Unlu MB, Gulsen G. An accelerated photo-magnetic imaging reconstruction algorithm based on an analytical forward solution and a fast jacobian assembly method. Phys Med Biol 2016;61(20):7448. [PubMed: 27694717]
31. Nouizi F, Erkol H, Luk A, Lin Y, Gulsen G. Analytical photo magnetic imaging. Optical Tomography and Spectroscopy OW4D–7. Optical Society of America; 2016.
32. Thayer DA, Lin Y, Luk A, Gulsen G. Laser-induced photothermal magnetic imaging. Appl Phys Lett 2012;101(8):083703.
33. Schweiger M, Arridge SR, Hiraoka M, Delpy DT. The finite element method for the propagation of light in scattering media: Boundary and source conditions. Med Phys 1995;22(11):1779–1792. [PubMed: 8587533]
34. Erkol H, Nouizi F, Unlu MB, Gulsen G. An extended analytical approach for diffuse optical imaging. Phys Med Biol 2015;60(13):5103. [PubMed: 26083326]
35. Arridge SR. Optical tomography in medical imaging. Inverse Probl 1999;15(2):R41.
36. Gibson A, Dehghani H. Diffuse optical imaging. Philos Trans R Soc A Math Phys Eng Sci 2009;367(1900):3055–3072.
37. Algarawi M, Nouizi F, Luk A, et al. High-resolution chromophore concentration recovery using multi-wavelength photo-magnetic imaging, Multimodal Biomedical Imaging XIV. 108710F. International Society for Optics and Photonics; 2019.
38. Ruiz J, Nouizi F, Cho J, et al. Breast density quantification using structured-light-based diffuse optical tomography simulations. Appl Opt 2017;56(25):7146–7157. [PubMed: 29047975]
39. Nouizi F, Torregrossa M, Chabrier R, Poulet P. Improvement of absorption and scattering discrimination by selection of sensitive points on temporal profile in diffuse optical tomography. Opt Express 2011;19(13):12843–12854. [PubMed: 21716527]

Author Manuscript Author Manuscript Author Manuscript Author Manuscript

40. Yalavarthy PK, Pogue BW, Dehghani H, Carpenter CM, Jiang S, Paulsen KD. Structural information within regularization matrices improves near infrared diffuse optical tomography. Opt Express 2007;15(13):8043–8058. [PubMed: 19547132]
41. Edjlali E, Bérubé-Lauzière Y. Solving analytically the simplified spherical harmonics equations in cylindrical turbid media. JOSA A 2018;35(9):1633–1644. [PubMed: 30182999]
42. Wissler EH. Pennes 1948 paper revisited. J Appl Physiol 1998;85(1):35–41. [PubMed: 9655751]
43. Bing C, Staruch RM, Tillander M, et al. Drift correction for accurate prf-shift mr thermometry during mild hyperthermia treatments with mr-hifu. Int J Hyperthermia 2016;32(6):673–687. [PubMed: 27210733]
44. Rieke V, Pauly KB. Mr thermometry. J Magn Reson Imaging 2008;27(2):376–390. [PubMed: 18219673]
45. Shah N, Cerussi A, Eker C, et al. Noninvasive functional optical spectroscopy of human breast tissue. Proc Natl Acad Sci 2001;98(8):4420–4425. [PubMed: 11287650]
46. van Veen RLP, Sterenborg HJCM, Pifferi A, Torricelli A, Cubeddu R. Determination of vis- nir absorption coefficients of mammalian fat, with time- and spatially resolved diffuse reflectance and transmission spectroscopy. Biomedical Topical Meeting. Optical Society of America; 2004.
47. Palmer KF, Williams D. Optical properties of water in the near infrared. JOSA 1974;64(8):1107–1110.
48. Unlu MB, Birgul O, Shafiiha R, Gulsen G, Nalcioglu O. Diffuse optical tomographic reconstruction using multi-frequency data. J Biomed Opt 2006;11(5):054008. [PubMed: 17092157]
49. Van Staveren HJ, Moes CJM, van Marie J, Prahl SA, Van Gemert MJC. Light scattering in intralipid-10% in the wavelength range of 400–1100 nm. Appl Opt 1991;30(31):4507–4514. [PubMed: 20717241]
50. Johnson AD, Sherwin K. Foundations of Mechanical Engineering. London: CRC Press; 1996.
51. Nouizi F, Erkol H, Luk A, Unlu MB, Gulsen G. Real-time photo-magnetic imaging. Biomed Opt Express 2016;7(10):3899–3904. [PubMed: 27867701]
52. Cerussi AE, Shah NS, Hsiang D, Durkin A, Butler JA, Tromberg BJ. In vivo absorption, scattering, and physiologic properties of 58 malignant breast tumors determined by broadband diffuse optical spectroscopy. J Biomed Opt 2006;11(4):044005. [PubMed: 16965162]
53. Quarto G, Spinelli L, Pifferi A, et al. Estimate of tissue composition in malignant and benign breast lesions by time-domain optical mammography. Biomed Opt Express 2014;5(10):3684–3698. [PubMed: 25360382]
54. Anderson PG, Kainerstorfer JM, Sassaroli A, et al. Broadband optical mammography: Chromophore concentration and hemoglobin saturation contrast in breast cancer. PLOS One 2015;10(3):e0117322. [PubMed: 25781469]
55. Choe R, Konecky SD, Corlu A, et al. Differentiation of benign and malignant breast tumors by in-vivo three-dimensional parallel-plate diffuse optical tomography. J Biomed Opt 2009;14(2):1–18.

Author Manuscript Author Manuscript Author Manuscript Author Manuscript

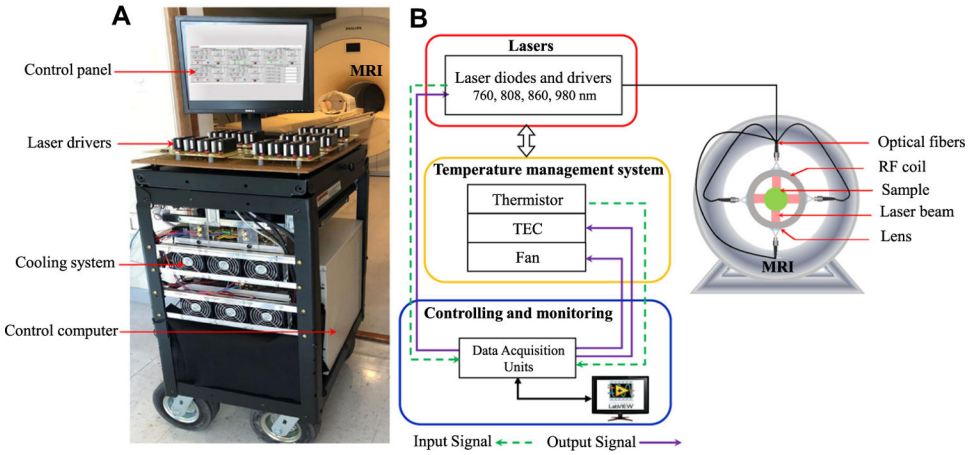

Fig. 1.

(A) Photography of the multi-wavelength photo-magnetic imaging system. **(B)** Schematic of the system showing the main components and their communication channels.

Author Manuscript Author Manuscript Author Manuscript Author Manuscript

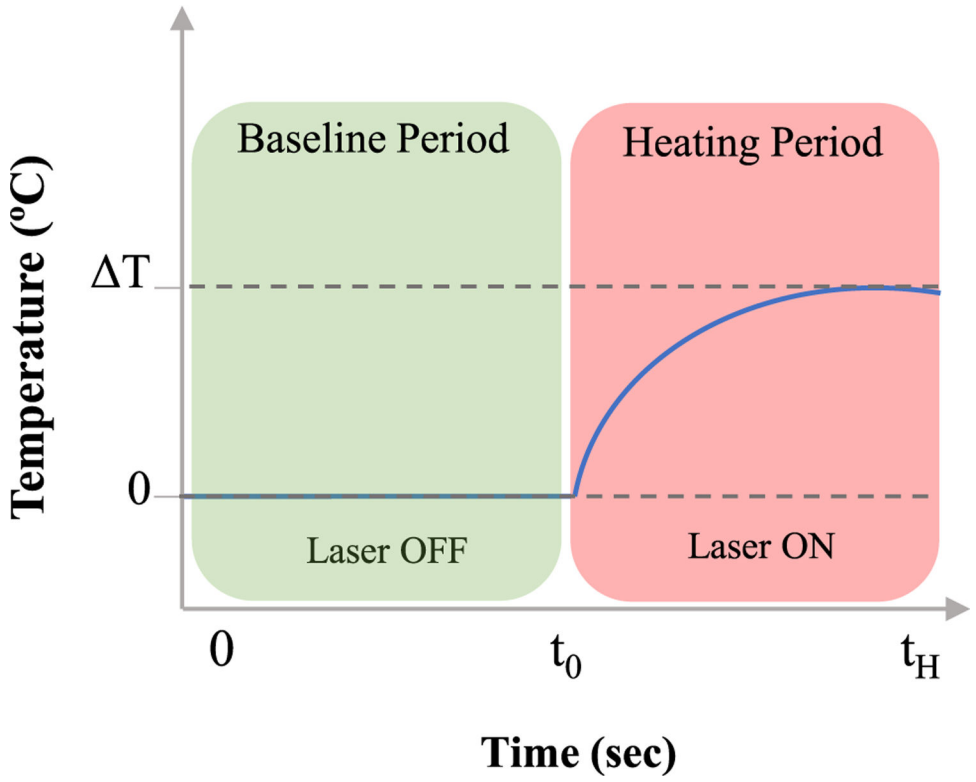

Fig. 2.
Magnetic resonance thermometry data acquisition timeline.

Author Manuscript Author Manuscript Author Manuscript Author Manuscript

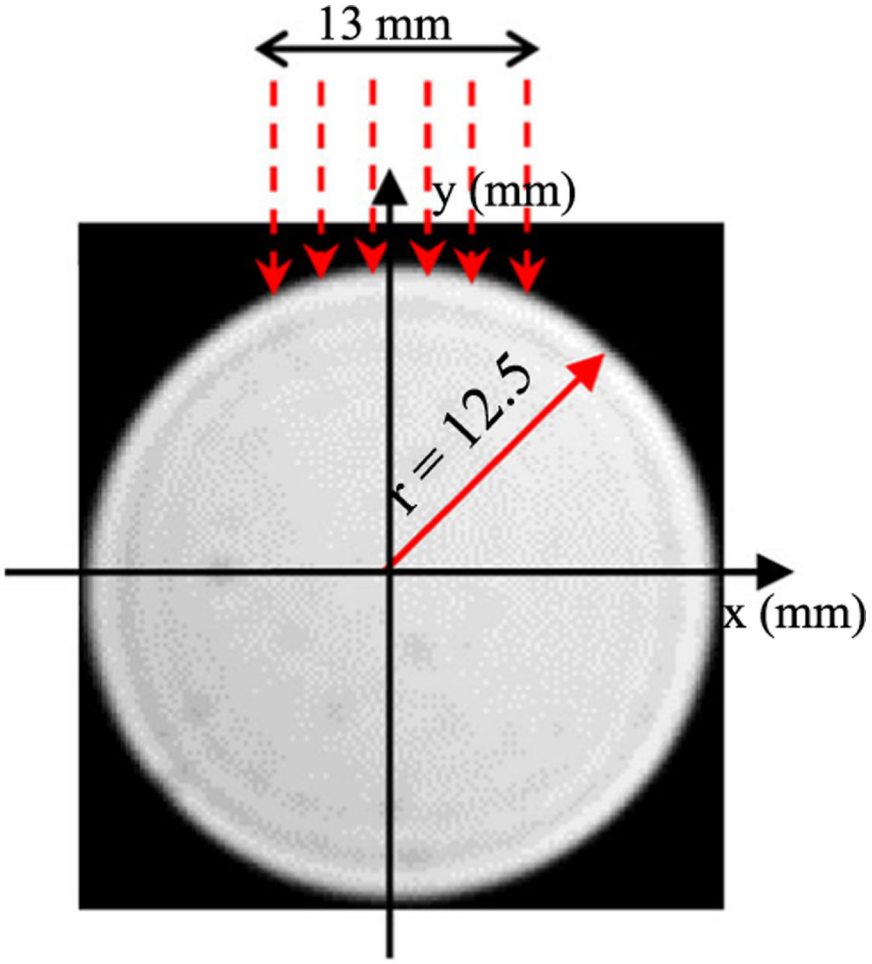

Fig. 3.

Axial T1-weighted magnetic resonance image of the 25 mm diameter phantom. The laser beam is illustrated using red dashed arrows at the top side of the phantom.

Author Manuscript Author Manuscript Author Manuscript Author Manuscript

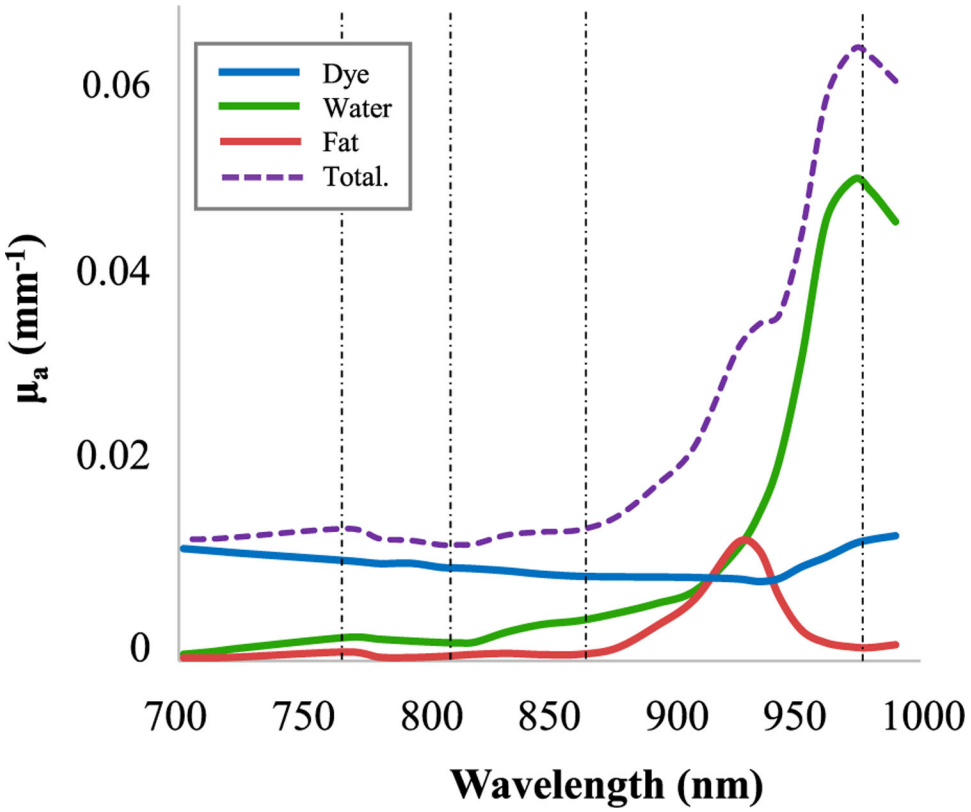

Fig. 4.

Total absorption spectrum of the phantom (dashed line) as well as its individual chromophores: water (green), lipid (red), and ink dye (blue) in the near-infrared spectral range. The vertical dot-dashed lines represent the wavelengths used in the study.

Author Manuscript Author Manuscript Author Manuscript Author Manuscript

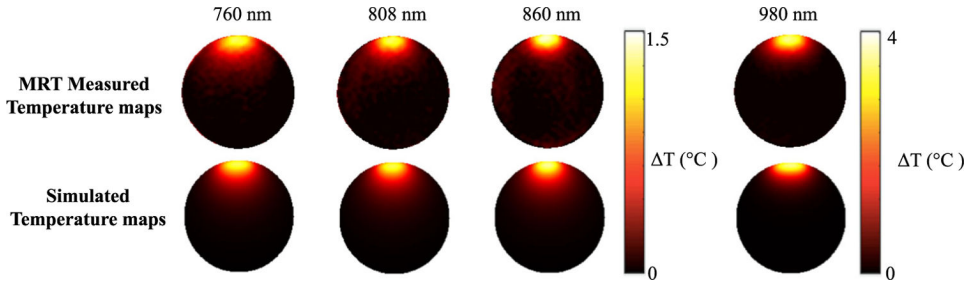

Fig. 5.

The magnetic resonance thermometry measured (first row) and simulated (second row) temperature maps after a 12 seconds heating period.

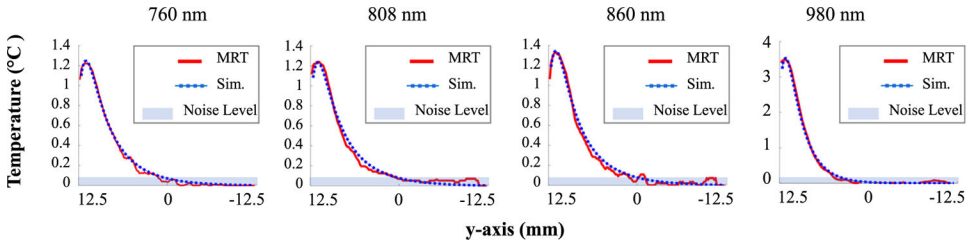

Fig. 6.

The profiles carried out along the *y*-axis of the induced temperature maps: magnetic resonance thermometry measured (red lines) and simulated temperatures (blue lines).

Author Manuscript Author Manuscript Author Manuscript Author Manuscript

Author Manuscript Author Manuscript Author Manuscript Author Manuscript

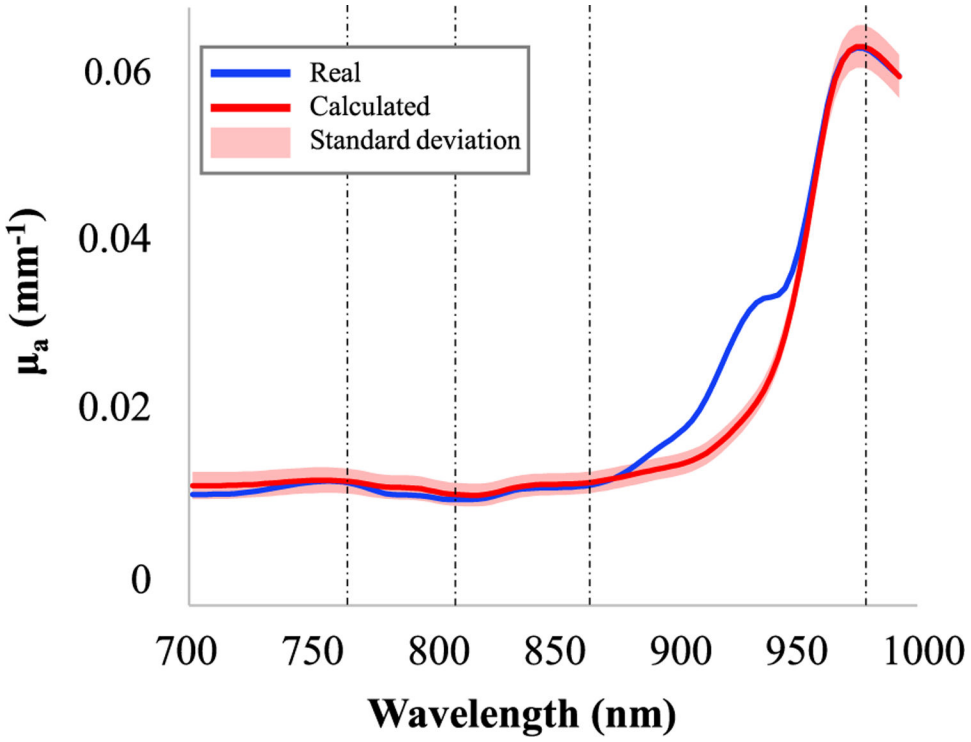

Fig. 7.

Total absorption spectrum of the phantom in the near-infrared spectral range: real (blue) and calculated (red). The highlighted red area represents the standard deviation of the recovered absorption, and the vertical dot-dashed lines represent the wavelengths used in the study.

Author Manuscript

Author Manuscript

Author Manuscript

Author Manuscript

TABLE 1.

The Real Optical Absorption and Reduced Scattering of the Phantom Used in the Study

Laser wavelengths (nm)	760	808	860	980
$\mu_a\,(\mathrm{mm}^{-1})$	0.0141	0.0124	0.014	0.0645
$\mu'_s(\mathrm{mm}^{-1})$	0.89	0.84	0.77	0.66

Author Manuscript

Author Manuscript

Author Manuscript

Author Manuscript

TABLE 2.

Thermal Properties of the Phantom Used in the Study

Parameters	Value	Units
Specific heat	4,200	$J{\cdot}(kg{\cdot}°C)^{-1}$
Thermal conductivity	6×10^{-4}	$W{\cdot}(mm{\cdot}°C)^{-1}$
Heat transfer coefficient	2×10^{-3}	$W{\cdot}(mm^{2}{\cdot}°C)^{-1}$
Density	1,000	$kg{\cdot}m^{-3}$

Author Manuscript Author Manuscript Author Manuscript Author Manuscript

TABLE 3.

The Mean, Standard Deviation and the Percentage Error of the Recovered Absorption Coefficient of the Phantom at all Four Wavelengths

Laser wavelength (nm)	**760**	**808**	**860**	**980**
Recovered μ_a (mm^{-1})	0.0144 ± 0.0011	0.0128 ± 0.0011	0.0142 ± 0.0008	0.065 ± 0.0028
Percentage error (%)	2.1	3.2	1.4	0.8

Lasers Surg Med. Author manuscript; available in PMC 2022 July 01.

Author Manuscript

Author Manuscript

Author Manuscript

Author Manuscript

TABLE 4.

The Real and Recovered Concentration of the Main Chromophores, Namely Water and the Used Ink Dye and Their Percentage Error

Chromophores	Water	Dye
Real concentration (%)	98	0.35
Recovered concentration (%)	98.38 ± 1.5979	0.39 ± 0.0465
Percentage error (%)	0.4	11.4